UC Santa Cruz
UC Santa Cruz Previously Published Works

Title

Explaining the Galilean Satellites' Density Gradient by Hydrodynamic Escape

Permalink

https://escholarship.org/uc/item/441259r2

Journal

The Astrophysical Journal Letters, 897(2)

ISSN

2041-8205

Authors

Bierson, Carver J
Nimmo, Francis

Publication Date

2020-07-10

DOI

10.3847/2041-8213/aba11a

Peer reviewed

Explaining the Galilean Satellites' Density Gradient by Hydrodynamic Escape

Carver J. Bierson[1], **Francis Nimmo**[1]

[1]Department of Earth and Planetary Sciences, UC Santa Cruz, 1156 High St, Santa Cruz, CA 95064, USA

Abstract

The Galilean satellites exhibit a monotonic decrease in density (and increase in ice mass fraction) with distance from Jupiter (Pollack & Fanale 1982). Whether this is because of the background conditions when they formed (Lunine & Stevenson 1982; Canup & Ward 2002; Mosqueira & Estrada 2003a; Ronnet et al. 2017), the process of accretion itself (Dwyer et al. 2013), or later loss due to tidal heating (Canup & Ward 2009), has been in dispute for forty years. We find that a hitherto largely neglected process - vapor loss driven by accretional heating (Kuramoto & Matsui 1994) - can reproduce the observed density trend for accretion timescales ≳300 kyr, consistent with gas-starved satellite formation models (Canup & Ward 2002, 2006). In this model both Io and Europa develop an early surface liquid water ocean. Vapor escape from this ocean causes the water inventories of Io and Europa to be completely and mostly lost, respectively. Isotopic fractionation arising from vapor loss means that Europa will develop a higher D/H ratio compared with Ganymede and Callisto. We make predictions that can be tested with in situ measurements of D/H of potential Europa plumes (Roth et al. 2014) by the Europa Clipper spacecraft, or infrared spectroscopic determinations (Clark et al. 2019) of D/H at all three bodies.

1. INTRODUCTION

There are three ways the compositional gradient among the Galilean satellites (Table 1) could have formed. One is that the gradient is determined by conditions in the proto-satellite disk: higher temperatures closer to Jupiter could result in an ice-poor or ice-free body, either because ice never formed (Pollack & Fanale 1982; Lunine & Stevenson 1982; Canup & Ward 2002; Mosqueira & Estrada 2003a) or because of sublimation of ice-rich particles (Ronnet et al. 2017). The rate at which material was supplied to the disk would have controlled the temperature distribution, the rate of satellite growth and inwards migration (Canup & Ward 2002); the present satellites may be only the final generation that survived inwards migration as the disk dissipated (Canup & Ward 2006). Second, higher impact velocities closer to Jupiter could have resulted in ice loss by physical erosion or vapor production; but this effect appears to be overwhelmed by radial mixing due to inwards migration (Dwyer et al. 2013). Last, subsequent effects which scale with semi-major axis, such as tidal heating (Canup & Ward 2009), could have removed volatiles later.

Corresponding author: Carver J. Bierson, cthomas1@ucsc.edu.

Models for satellite growth fall into two categories. If all the solid material is present in the proto-satellite disk at the same time, satellite growth is rapid, typically tens to thousands of years (Lunine & Stevenson 1982; Mosqueira & Estrada 2003a). Conversely, if material is fed slowly into the disk, surface densities are lower and growth timescales longer, 100 kyr or more (Canup & Ward 2002). Slow growth timescales are required to explain a Callisto that is not fully differentiated (Barr & Canup 2008); however, its actual differentiation state is not certain (McKinnon 1997).

Below we propose a new mechanism for generating the compositional gradient during accretion. Warm temperatures in the inner part of the disk combined with energy deposited during satellite accretion lead to a surface water ocean. The resulting water atmosphere can be rapidly lost via hydrodynamic escape (Lehmer et al. 2017) leading to the range of observed densities and predictions for isotopic fractionation of H and O.

1.1. Energy Balance

We consider the evolution of a satellite forming in the presence of a background disk using an energy balance approach. The disk is heated internally by viscous dissipation and is assumed optically thick; the disk temperature, pressure, and density all decrease with distance from Jupiter (Lunine & Stevenson 1982; Canup & Ward 2002). We assume that the material being accreted to the satellite is at the same temperature as the local disk. Energy is delivered to the growing satellite surface in two forms. The first is radiation from the background disk; the second is gravitational energy delivered by impacts, where the rate of growth depends on the accretion timescale τ (see Appendix A). The newly accreted material is not necessarily at the same temperature as the satellite's surface. If the accreted material is warmer than the satellite's surface, it will act as an additional source of energy, or conversely a sink if it is colder (as is more often the case). Our model implicitly assumes that accretion is dominated by bodies small enough to be approximated by continuous accretion but large enough to not deposit their energy in the disk or atmosphere. This is intermediate between other models such as Ronnet et al. (2017) who assume cm sized particles, and Canup & Ward (2006) who assume larger impactors dominate.

This incoming energy goes into two main processes. The first is heating or cooling of a surface layer (of thickness z). If the surface temperature excceds the melting temperature of water a surface ocean will create an atmosphere around the satellite in saturated vapor pressure (SVP) equilibrium (Lehmer et al. 2017, Appendix A). Because of the low surface gravity of the growing satellite, the water vapor atmosphere can be rapidly lost via hydrodynamic escape. This loss is the second major energy sink.

Quantitatively, the processes identified above are described by the following equation:

$$\frac{GM\dot{M}}{r} - 4\pi r^2 \sigma\left(T^4 - T_B^4\right) - c_p\dot{M}(T - T_B) = c_p\rho\frac{4}{3}\pi\left(r^3 - [r - \min(r, \Delta z)]^3\right)\dot{T} + \Phi$$
$$(T, g)\left(L_v + \frac{GM}{r}\right)$$

(1)

Here $M(t)$ and $r(t)$ are the satellite mass and radius, T and T_B the surface and disk temperatures, c_p the specific heat capacity, ρ the density, Φ the rate of atmospheric loss, L_v

the latent heat, g the surface gravity and dots denote time-derivatives. From left to right the terms represent: gravitational potential energy; surface radiation; heat content of the accreting material; heating of the near-surface; and atmospheric (hydrodynamic) escape. This model is not sensitive to the thickness of the near-surface layer, z, so long as it is much smaller than the body radius (Section D.3). Similarly, we bound the results by assuming an atmospheric temperature structure which is either isothermal or saturated (Lehmer et al. 2017). These equations are based on the model of Kuramoto & Matsui (1994); further details and discussion of parameter choices may be found in Appendix A and Table 2.

Hydrodynamic escape occurs when the bulk atmosphere is lost via a vertical wind that is driven by the pressure difference between the surface and background. The vertical wind velocity starts low near the surface but then accelerates to the sound speed at the so-called critical point (Lehmer et al. 2017). Escape is highly efficient for low gravity, high temperature worlds but can be eliminated if the background pressure is sufficiently high (Young et al. 2019).

The primary prediction we can make with this model is the isotopic difference in the water inventory of Europa, Ganymede, and Callisto. In hydrodynamic escape there is very little fractionation between species with small mass differences that are both part of the escaping flow (Zahnle & Kasting 1986). There is, however, fractionation between the ocean and atmosphere. Because the difference in the absolute isotopic ratios, R, are small we use the delta notation

$$\delta = \left(\frac{R - R_{std}}{R_{std}} \right) \times 10^3 . \tag{2}$$

Throughout the text we use δD for deuterium to hydrogen ratio and $\delta^{18}O$ for the ^{18}O to ^{16}O ratio. Full details on the fractionation modeling are given in Section B.

2. RESULTS

2.1. Example model run

Figure 1 show an example model run output. This particular example produces a satellite slightly more ice rich than Europa but is a good illustration of the processes involved. This figure shows metrics for the growth of the satellite (r, M), the conditions at the surface (T and the upwards velocity of the escaping atmosphere u), and the integrated quantities (bulk density ρ_S and isotopic fractionation δD). The distance to the critical radius (r_c/r) is a measure of the strength of hydrodynamic escape where larger values correspond to less escape (Tian et al. 2005).

For the model in Figure 1, the background temperature is 200 K. As this is below the melting point, the energy of accretion initially goes into warming the surface. Once the surface temperature reaches the melting point, an atmosphere forms and escape begins. Initially escape is efficient (because of the low surface gravity) and is limited by the rate of energy delivery. At about 5 kyr the surface gravity becomes the limiting factor for escape,

and the excess energy now begins to warm the surface. Once accretion finishes (~7.5 kyr) the energy source driving escape is lost and the surface temperature quickly returns to the background temperature.

There are two key factors that control the isotopic fractionation: the loss rate compared to the accretion rate, and the surface temperature. At the start of accretion, the satellite is losing material quickly and the temperature is relatively low leading to efficient fractionation. As the satellite develops significant surface gravity the escape rate decreases while non-fractionated material is still being accreted (and mixed). In addition, as the temperature rises there is less fractionation between the ocean and atmosphere. The net effect is that δD begins to relax back towards the background value. These processes combine to produce a fractionation curve that peaks before accretion is complete (Figure 1d). Oxygen isotopes will behave in an analogous way and the predicted values for oxygen are presented in Appendix E.

2.2.   Using inputs from Canup and Ward 2002

Figure 1 shows that a Europa-like outcome can be obtained for suitable parameter choices. Since the different satellites experienced different disk conditions (pressure and temperature), we next investigate whether a self-consistent set of parameters can produce analogues to all four bodies. For this example we use the "gas-starved" disk model of Canup & Ward (2002). The key parameters in this model are the disk turbulence, α, and the accretion rate of Jupiter, $M_J\dot{M}$. In Figure 2 we use the same values as Figure 6 of Canup & Ward (2002). Fig 2a shows the disk parameters derived, and Fig 2b shows the calculated final satellite density as a function of distance. For these calculations we use three different satellite accretion timescales. For accretion timescales between 300 kyr and 1 Myr the calculated density trend agrees with the observed values, neglecting any satellite migration (see below). The agreement between our model density values and those observed is striking. Fig 2c shows that Europa is expected to have a δD~20 relative to the accreted material, in line with what was presented in Figure 1.

2.3.   Parameter space exploration

To understand the processes in this model more generally, we look at where in parameter space we can match the density of the Galilean satellites. Figure 3 shows the final density as a function of T_B and accretion timescale τ for objects that would have a final radius R_f of 2000 km if no mass loss occurred. The solid lines on these plots are contours of the density for Europa, Ganymede, and Callisto. The four panels show different model assumptions about the atmospheric temperature structure (isothermal or saturated) and the background disk pressure (p_B =0.0 Pa or p_B =1.0 Pa). As expected, switching to a saturated temperature structure and adding a background pressure both reduce the mass lost. The key finding, however, is that in all cases we can reproduce the density of all four Galilean satellites by appealing to a common accretion timescale as long as it is sufficiently slow (τ >300 kyr). When using a larger final radius of R_f= 2500 km (more representative of Ganymede and Callisto) this general result still holds (Figure 8). The expected shorter accretion timescale (by a factor of a few) of the inner moons would not affect our conclusions significantly.

Figure 3 can be roughly divided into two regimes. For short accretion timescales the delivery rate of accretion energy is large and the amount of time over which escape occurs is short. As a result, the final density is more sensitive to the total mass accreted (See Figure 8). For long accretion times the warming from the background disk is much more important because vapor loss rates are integrated over a longer period of time. This leads to a stronger dependence of the final density on the background temperature.

Figure 4 shows the δD values predicted by our model for Europa, Ganymede, and Callisto across our parameter space. We also plot what would be expected if Europa initially accreted all its ice and then lost 88% of it from some water-vapor fractionation process (Rayleigh distillation - see Appendix B). Our hydrodynamic model predicts that Europa should have $\delta D < 100$. In contrast if Europa accreted the same amount of water as Callisto and then lost it via Rayleigh distillation we expect $\delta D > 100$. It is important to note that the absolute δD values reported assume that all three satellites accreted from material that had the same initial D/H (of VSMOW). The actual δD of the material that formed the Galilean satellites is unknown and thus we emphasize the difference among the satellites, not the absolute value of δD. The same process and discussion applies to the oxygen isotopes (Figure 11). Our model predicts a difference of $\delta^{18}O \sim 3$ while Rayleigh fractionation predicts $\delta^{18}O \sim 30$.

3. DISCUSSION

Our model only forms objects having a density comparable to Ganymede and Callisto with accretion timescales longer than $\gtrsim 300$ kyr. This is because faster formation timescales result in at least some mass loss for low background temperatures. There are two possible interpretations of this result. The first is that Ganymede and Callisto did accrete rapidly, but started more ice-rich than we assumed, developing an initial ocean and losing some H_2O as they grew. However, none of the icy worlds in the solar system with a radius larger than 1000 km has a bulk density lower than 1800 kg/m^3. Furthermore, at least on Callisto, there is no global network of extensional fractures that would be predicted from the refreezing of a primordial ocean (Moore 2006). The second interpretation, which we favor, is that the satellites formed on a timescale $\gtrsim 300$ kyr. This is consistent with the gas-starved model of satellite growth (Canup & Ward 2002) and with a potentially undifferentiated Callisto (Barr & Canup 2008). This would also imply that the observed differences between Ganymede and Callisto are not due to their formation but rather to their subsequent evolution. For instance, Ganymede likely underwent heating episodes during its evolution into the current Laplace resonance with Io and Europa (Showman et al. 1997).

The potential development of an initial surface ocean on Europa was also noted by Lunine & Stevenson (1982). Such an ocean would likely have accumulated organic material during accretion, and would have resulted in enhanced tidal dissipation. Whether Europa's present-day ocean is a remnant of this primordial ocean is unclear, but if so then it would have experienced prolonged hydrothermal interactions with the silicates beneath (Vance et al. 2007).

The absence of a correspondingly orderly density gradient in the Saturnian satellites is intriguing. In our model water loss is most efficient when background temperatures are high

and the satellites are small. Thus, the fact that Titan (large and distant) has a similar ice content to Ganymede or Callisto is easy to explain. Conversely, the small ice-rich inner satellites like Tethys are hard to explain, since protoplanetary disk temperatures were probably too warm for ice (Mosqueira & Estrada 2003b). Most likely these satellites represent either late-formed bodies when the gas was thin (Mosqueira & Estrada 2003b) or gone (Charnoz et al. 2011); alternatively, they may be disrupted fragments from some much later catastrophe (Asphaug & Reufer 2013).

Figures 2 and 3 show that the disk temperatures and satellite growth times predicted by the gas-starved model can reproduce the observed density gradient. Our results, however, are simplified in at least two important ways. First, we ignore satellite migration, and, second, we neglect the changing conditions in the disk. The extent of inwards migration is currently unclear, since migration can stall if satellite-satellite resonances are established (Canup & Ward 2006; Ogihara & Ida 2012). With regards to the background temperature (T_B), the value used in this model may be thought of as the local, temporally averaged, temperature of the disk during satellite growth. Future work coupling the disk evolution and satellite growth would provide further insight into the importance of these processes.

We have argued above that accretion-derived hydrodynamic escape can naturally produce the observed densities of the Galilean satellites. Furthermore, we predict that this will result in modest fractionation of H and O at Europa compared with Ganymede and Callisto. Mass spectrometer and spectroscopic measurements (Clark et al. 2019) by the forthcoming JUICE and Europa Clipper missions will test these predictions in the coming decade. While here we have focused on isotopes, further work on other volatile species or the hypothesized early ocean of Europa could lead to more predictions that will help elucidate the origin of this system.

ACKNOWLEDGMENTS

APPENDIX

Appendix

Table 2.

Symbols used in this work. Dots over terms throughout the text indicate time derivatives. Terms that use the f subscript indicate the final value ignoring escape (i.e. R_f is the final radius if no mass was lost). Parameters with specific values are given in table 3

Symbol	Value	Units
M	Mass	kg
r	radius	m
T	Temperature	K

T_B	Background Temperature	K
T_m	Melting temperature	K
G	Gravitational Constant	$m^3 \, kg^{-1} \, s^{-2}$
g	Gravitational acceleration	$m \, s^{-2}$
c_p	Specific heat of satellite	$J \, kg^{-1} \, K^{-1}$
L_v	Latent heat of vaporization	$J \, kg^{-1}$
σ	Stefan Boltzmann constant	$W \, m^{-2} \, K^{-4}$
ρ	Solid density	$kg \, m^{-3}$
z	Thickness of surface layer	m
Φ	Mass loss rate	$kg \, s^{-1}$
u	Vertical velocity	$m \, s^{-1}$
R_{gas}	Ideal gas constant	$J \, mol^{-1} \, K^{-1}$
M_g	Molar mass of gas	$kg \, mol^{-1}$
R	Specific gas constant (R_{gas}/M_g)	$J \, kg^{-1} \, K^{-1}$
p	Atmosphere pressure	Pa
p_{sat}	Saturation vapor pressure of H_2O	Pa
γ	Evaporation coefficient	-
J	Evaporation rate	$kg \, s^{-1} \, m^{-2}$

	Subscripts
S	Satellite
B	Background
c	Critical point
i	Ice
g	Gas
r	Rock
l	Liquid
f	Final (ignoring mass loss)

A.: NUMERICAL APPROACH

Our model is based on the energy balance model of Kuramoto & Matsui (1994). The symbols used throughout this work are described in Table 2. The primary energy balance is as follows

$$\underbrace{\frac{GM\dot{M}}{r} - 4\pi r^2 \sigma\left(T^4 - T_B^4\right) - c_p \dot{M}(T - T_B)}_{E_{excess}} = \underbrace{c_p \rho \frac{4}{3}\pi\left(r^3 - [r - \min(r, \Delta z)]^3\right)\dot{T}}_{E_{\dot{T}}}$$
$$+ \underbrace{\Phi(T, g)\left(L_v + \frac{GM}{r}\right)}_{E_{escape}} \tag{A1}$$

It is useful to think of Eqn. A1 as consisting of three parts. The left hand side, E_{excess}, accounts for the energy sources and sinks dependent on the current state of the forming satellite (t, T, M, r). The three terms in E_{excess} correspond to the gravitational energy of

accretion, the surface radiation balance, and the energy required to warm newly accreted material to the current surface temperature. We assume that the surface temperature is the effective radiating temperature, appropriate for an optically thin atmosphere. Further discussion of the atmospheric temperature structure is provided below. The right hand side terms are the satellite response, and thus change the state variables, either T or M respectively. There are three regimes for this equation

1. $T < T_m$: This represents a satellite which has not yet warmed enough to have a surface ocean. In this case E_{excess} all goes into warming or cooling the surface.

2. $T \approx T_m$ & $E_{excess} > E_{escape}$: In this case the satellite has a surface ocean and is losing mass via hydrodynamic escape. The incoming energy in this case exceeds the energy lost to escape and so the surface temperature continues to rise.

3. $T > T_m$ & $E_{excess} < E_{escape}$: Here the satellite still has a surface ocean and is losing mass. In this case however the surface temperature will drop to provide extra energy for escape. If the surface temperature drops below T_m escape ceases. In these cases the escape rate will be limited by E_{excess}

By prescribing $\dot{M}$, Equation 1 can be solved for $\dot{T}$ given a known function for $\Phi(T, g)$. The form of $\dot{M}$ used in this study is (Safranov 1972; Kuramoto & Matsui 1994)

$$\dot{M} = \begin{cases} 7.15\left(\dfrac{M_S}{M_f}\right)^{2/3}\dfrac{M_f - M_S}{\tau}, & M_S + M_L < M_f \\ 0, & M_S + M_L \geq M_f \end{cases} \tag{A2}$$

Here M_L is the mass lost, such that at the end of accretion $M_f - M_L = M_S$. This form was chosen because it provides a nearly constant $\dot{r}_S$ for most of accretion that slows down as the body nears its final size. This reduces the discontinuity in $\dot{M}$ as accretion finishes. Because τ is varied by order of magnitude there is very little sensitivity to the exact form of $\dot{M}$.

Φ is the mass loss rate and can be related to the vertical velocity and atmospheric density via

$$\Phi = 4\pi r^2 \rho_g u \tag{A3}$$

Due to continuity, Φ is the same at all altitudes. We assume the surface atmospheric density (ρ_g) at the surface is given by the saturated vapor pressure (SVP) of water (Lehmer et al. 2017). We solve for u at the surface using the hydrodynamic equations (Lehmer et al. 2017):

$$\frac{1}{\rho_g}\frac{\partial \rho}{\partial r} + \frac{1}{u}\frac{\partial u}{\partial r} + \frac{2}{r} = 0 \text{ Continuity} \tag{A4}$$

$$u\frac{\partial u}{\partial r} + \frac{1}{\rho_g}\frac{\partial p}{\partial r} = -\frac{GM_S}{r^2} \text{ Force Balance} \tag{A5}$$

$$p = \rho_g RT \text{ Equation of state} \tag{A6}$$

These can be combined and rewritten as

$$\frac{\partial u}{\partial r} = \frac{u}{u^2 - RT}\left[\frac{2RT}{r} - R\frac{\partial T}{\partial r} - \frac{GM_S}{r^2}\right] \tag{A7}$$

$$\frac{\partial \rho_g}{\partial r} = \frac{-\rho_g}{u^2 - RT}\left[\frac{2u^2}{r} - R\frac{\partial T}{\partial r} - \frac{GM_S}{r^2}\right] \tag{A8}$$

Because the vertical velocity at the critical point is known to be the sound speed ($\sqrt{RT}$), we can integrate Equation A7 from r_c the surface to obtain the surface velocity. This was done using the ODE solver of Shampine & Gordon (1975). Thus all terms in Eqn. A3 are known for the surface.

To solve Equation A7 requires knowledge of $\partial T/\partial r$. For modern solar system bodies this is often done by solving for the temperature structure of the atmosphere (Tian & Toon 2005). For these forming satellites there are large uncertainties associated with calculating the temperature structure and thus we opt to use two bounding temperature structures, isothermal and saturated (Lehmer et al. 2017). As can be seen from equation A7, the isothermal case produces the maximum escape rate. In contrast the saturated atmosphere is the shallowest temperature structure for a water vapor atmosphere and thus provides the minimum escape rate (Lehmer et al. 2017). The detailed numerical methods for the saturated case are presented in Appendix D.2z.

There are two special cases in which the escape is limited. The first is when there is no water left on the forming satellite. This is tracked by having the satellite density evolve self-consistently as water is lost. When the bulk water fraction equals zero the escape is set to zero. The second case is when the atmospheric pressure at the critical point approaches the background pressure of the disk (Young et al. 2019). By combining Equation A3, which is constant with altitude, with the ideal gas law, we can calculate the atmospheric pressure at the critical point. We reduce the escape rate by

$$\Phi = \Phi(T, g)\left(1 - e^{-p_c/p_B}\right) \tag{A9}$$

where p_c is the atmospheric pressure at the critical point. This has nearly the same effect as setting the escape rate to zero when the pressure at the critical point drops below the background pressure. Using an exponential decay, as opposed to a hard limit, prevents numerical oscillations which would otherwise occur around that limit.

Table 3.

Model Parameters used

Symbol	Value
ρ_r	3500 kg m^{-3}
ρ_i	920 kg m^{-3}
ρ_B	1800 kg m^{-3}
z	10 km

Symbol	Value
L_v	2.5×10^6 J kg^{-1}
c_p	1300 J kg^{-1} K^{-1}
R_{std}	1.5575×10^{-4}

Because the surface pressure is an important factor in calculating the escape rate, we check that two requirements are met that allow us to assume SVP. We require that the escape rate is not faster than the rate at which the ocean can evaporate, and that the e-folding timescale for the satellite to reach SVP is much less than our model accretion timescale. Following (Young et al. 2019) we calculate the evaporation rate as

$$J = \frac{M_g \gamma (p_{\text{sat}} - p)}{\sqrt{2\pi M_g R_{gas} T}} \tag{A10}$$

Here J is the evaporation rate in kg s^{-1} m^{-2} and γ is a constant sticking coefficient. Taking γ = 0.3 (Mozurkewich 1986) we find that the evaporation rate is generally three orders of magnitude faster than escape rate. The e-folding timescale for the atmosphere to reach SVP is around 30 minutes. Given these values we find that the assumption of surface SVP is justified.

A key parameter in this study is the density (or equivalently the ice fraction) of the accreted material. We chose a nominal value of 1800 kg m^{-3}. This value is comparable to the density of Ganymede and Callisto. It is also comparable to the density of other large icy worlds ($r >$ 1000 km) in the outer solar system namely Titan (1880 kg m^{-3}), Triton (2050 kg m^{-3}), and Pluto (1854 kg m^{-3}). The fact that none of these large outer solar system worlds have a bulk density lower than 1800 kg m^{-3} indicates that this density is representative of the material these worlds formed from. Many of the smaller worlds ($r <$ 1000 km) in the outer solar system have a lower bulk density, however this has been interpreted as being due to large bulk porosity (Malamud & Prialnik 2015; Bierson & Nimmo 2019; Castillo-Rogez et al. 2019).

All model results in this text are shown after one accretion timescale (τ) has elapsed. In nearly all cases allowing the model to run longer has no impact on the results because there is no more energy of accretion. The one exception is when the background temperature is high enough to drive escape independent of the gravitational energy of accretion, but the accretion time is short enough that not all the water is lost in one τ. Canup & Ward (2006) found that, in a gas starved disk, if satellites become too massive they drift inwards and collide with the central planet causing multiple generation of satellites to form. For this work we are only interested in the final generation of satellites as those are the ones we observe. For that final generation, the end of accretion is assumed to correspond with the removal of the proto-Jovian disk and thus the viscous heat source for the background temperature.

B.: ISOTOPE FRACTIONATION

Isotopic fractionation is typically measured as a ratio. In the case of hydrogen and deterium this ratio is defined as

$$R = \frac{D}{H}.$$ (B11)

When the liquid and vapor phases are in equilibrium their relative ratios can be defined by

$$\alpha(T) = \frac{R_g}{R_l}.$$ (B12)

The parameter α is strongly temperature dependent such that at higher temperatures more of the heavy isotope will be in the gas phase. In this work we use the experimentally measured values of α from (Horita & Wesolowski 1994).

For each model timestep, two processes affect the satellite isotopic ratio. The first is the addition of new material mixing with the existing reservoir. This is calculated by a mass-weighted mixing of the two ice reservoirs.

$$R_S = \frac{M_{i,S}R_S + M_{i,B}R_B}{M_{i,S} + M_{i,B}}$$ (B13)

After this material is mixed, fractionation occurs due to the atmospheric mass loss. Within each timestep this is treated as Rayleigh distillation. Rayleigh distillation assumes that the ocean and atmosphere are able to achieve isotopic equilibrium as the atmosphere is progressively removed. This equilibrium is justified by the fact that the evaporation timescales are much faster than the loss timescales (see Appendix A). This is calculated by

$$R_S = R_S^0 \left(\frac{M_{i,l}}{M_i}\right)^{\alpha(T) - 1}$$ (B14)

Because variations in R are small it is useful to define

$$\delta D = \left(\frac{R - R_{std}}{R_{std}}\right) \times 10^3.$$ (B15)

Given the large uncertainty we treat the background R and R_{std} as that of SMOW (Table 3). The focus of this however is not the absolute value of R but the relative difference between model satellites of varying composition.

B.1. Fractionation due to hydrodyanmic escape

The other possible source of isotopic fractionation is direct fractionation during the escape process. This has been widely modeled for early Earth and Venus where an initial H_2 atmosphere may have fractionated the noble gases during hydrodynamic escape (Hunten 1973; Zahnle & Kasting 1986). Following Zahnle & Kasting (1986) we can estimate α for hydrodynamic escape as

$$1 - \alpha \approx \left(\frac{m_i}{m} - 1\right)\left(\frac{m}{m_i} \frac{\phi r^2 RT}{GM b_i}\right) \tag{B16}$$

where ϕ is the loss flux (molecules m^{-2} s^{-1}), m is the mean molar mass of the escaping flow, m_i is the molar mass of the species being fractionated, and b_i is the binary diffusion coefficient (molecules m^{-1} s^{-1}). To estimate typical values for hydrodynamic escape we will parameterize the escaping flux as the total mass lost over the accretion timescale and a characteristic radius

$$\phi \approx 4 \times 10^{21} \text{ molecules m}^{-2}\text{s}^{-1}\left(\frac{M_L}{5 \times 10^{22}\,\text{kg}}\right)\left(\frac{1000\,\text{km}}{r}\right)^2\left(\frac{10^6\,\text{yrs}}{\tau}\right) \tag{B17}$$

For more intuition we substitute GM/r^2 with the gravitational acceleration g. This provides characteristic values of

$$1 - \alpha \approx 10^{-7}\left(\frac{\phi}{4 \times 10^{21} \text{ molecules m}^{-2}\text{s}^{-1}}\right)\left(\frac{T}{300\,\text{K}}\right)\left(\frac{0.5\,\text{m s}^{-2}}{g}\right)$$
$$\left(\frac{b_i}{3 \times 10^{21} \text{ molecules m}^{-1}\text{s}^{-1}}\right) \tag{B18}$$

Typical values for $1 - \alpha$ due to evaporation depending on temperature are 0.01–0.2. The reason the hydrodynamic escape factor α is so low when compared with the terrestrial literature is the escape rate here is much faster and the mass difference between the mean flow and fractionating species is much smaller. Because no relevant choice of parameters would cause the fractionation due to escape to be comparable to that of evaporation we ignore it in this work.

C.: PROCESSES NOT MODELED

While the surface ocean is assumed when the satellite surface temperature exceeds the melting temperature we do not explicitly track that oceans' properties. This includes the ocean thickness or the water-ice ratio. Because of this we do not include the latent heat involved as the surface ocean melts or refreezes because this is all within the satellite system (i.e. no energy is gained or lost from the satellite). We do include the latent heat for any water that escapes (see Equation 1).

In our model we parameterize the outgoing longwave radiation (OLR) as perfect blackbody radiation (σT^4). It has been observed that the Earth's OLR is linear with temperature. This has been attributed to the the increased thickness of water vapor absorption lines as the temperature increases (Koll & Cronin 2018). This mechanism depends on a large reservoir of water allowing the atmosphere to equilibrate. At temperatures above ~300 K the atmosphere becomes opaque to infrared radiation and a greenhouse state is encountered. At this point the OLR becomes almost independent of the surface temperature. As the temperature rises the radiating level rises to allow slightly more energy to escape. The key point as it relates to this work is that an atmosphere with access to a water reservoir radiates less energy than would be predicted by σT^4.

Given the above and the temperatures in our model the forming Galilean satellites could be in this linear OLR regime. This would mean less energy radiated away from the system and more energy available to warm the surface, potentially leading to more escape. Unlike the Earth system however much of the incoming radiation is likely also in the infrared (because the proto-Jovian disk is opaque). Therefore as the spectral windows narrow, both the incoming and outgoing energy will begin to be limited. The net effect of this process is not entirely clear and should be explored in future work.

Also not included in this model are the effects of clouds. The presence of clouds will also affect the incoming energy budget. Clouds also affect the atmospheric temperature structure, however, so long as it is a water vapor atmosphere, the temperature profile should not drop below the saturated limit used in this work.

In our model, the surface temperature generally is static or rises throughout the accretion process. As accretion progresses this leads to an internal thermal structure with the highest temperatures near the surface. In this case thermal diffusion would cause some heat to leak inwards towards the body center. The rate of energy loss however is very slow when compared to the other terms. For example a temperature contrast of 300 K in a layer 10 km thick and $r = 1500$ km leads to a leakage rate of $\sim 10^{12}$ W. This is several orders of magnitude less than the other energy terms (Figure 5).

Radioactive decay as an energy source is also not included. All the energy sources discussed in this model are focused in the near-surface layer. In contrast the energy release from radioactive decay is distributed throughout the silicate part of the body. While the total energy released by radioactive decay is much larger than these energy sources, the power delivered in the near surface is much smaller. For reference, the power released from radioactive decay of ^{26}Al in the top 10 km of a 1500 km body with 70% rock mass fraction at the time of CAI formation is $\sim 10^{14}$ W. For comparison (as show in Figure 5) the energy terms leading to escape in our models are typically $\gg 10^{16}$ W. Thermal diffusion would allow some of this heat to be transported to the surface but this is generally slower than the timescales considered in this work.

A term that could also lead to more loss is the additional gravitational energy from Jupiter's tidal potential. In this work we neglect this term because it requires an assumption both of Jupiter's growth rate relative to the satellites and the distance at which each satellite formed.

We assume the temperature and pressure of the disk are constant over the formation time of the satellites. For long formation times this is likely not the case as the disk conditions will evolve (Alibert et al. 2005). The goal of this study is to test the validity of our proposed mechanism. Thus we chose to show the model dependence on these key parameters (T, p) by assuming constant values, rather than linking our results to a specific disk model.

In this work we assume that the accreted mass is large enough to deposit its energy at the surface but small enough to be approximated as a continuous stream of material. If the material is smaller than we assume some fraction of the energy will be directly deposited into the atmosphere. Note that this requires that the surface is warm enough to sustain that atmosphere and so escape would still be occurring. The exact fraction of energy deposited

into the atmosphere and radiated during ablation would depend on the size of the particles in addition to the mass and opacity of the atmosphere.

If the material being accreted is much larger than we assume the heat may be deeply buried. In this case we have to consider how that heat is transported to the surface. If the heat can only be conductively transported the surface may stay too cold to support large amounts of escape. In contrast, if the heat is advectively transported (e.g. by porous water flow) the result may be very similar to the results presented in this work. Which style of heat transport is active would likely depend on the frequency of impacts (and therefore the accretion timescale).

In both the small and large size limit similar processes would likely be active to those discussed in the text but with the energy efficiency reduced. Determining the magnitude of that efficiency reduction would require more knowledge of both the incoming material (e.g. its size distribution) and the forming satellites.

D.: CONSERVATION AND SENSITIVITY METRICS

D.1. Energy Conservation

Figure 5 shows the evolution of the energy terms over a model run. This model run used the parameters $R_f = 2500$ km, $\tau = 10^4$ years, $T_B = 200$ K. We quantify the fractional energy conservation as

$$E_{error} = \frac{E_{excess} - E_{evolve}}{E_{excess}} \qquad \text{(D19)}$$

where E_{excess} and E_{evolve} are the left and right side of Equation 1 respectively. The median error is exactly 0.0 with 16 significant digits and the mean is ~10^{-2}%. The worst energy conservation is always in the time step when accretion ends. Here E_{error} can peak to values ~1%. During this phase however little to no mass is lost and so the impact on our results is negligible.
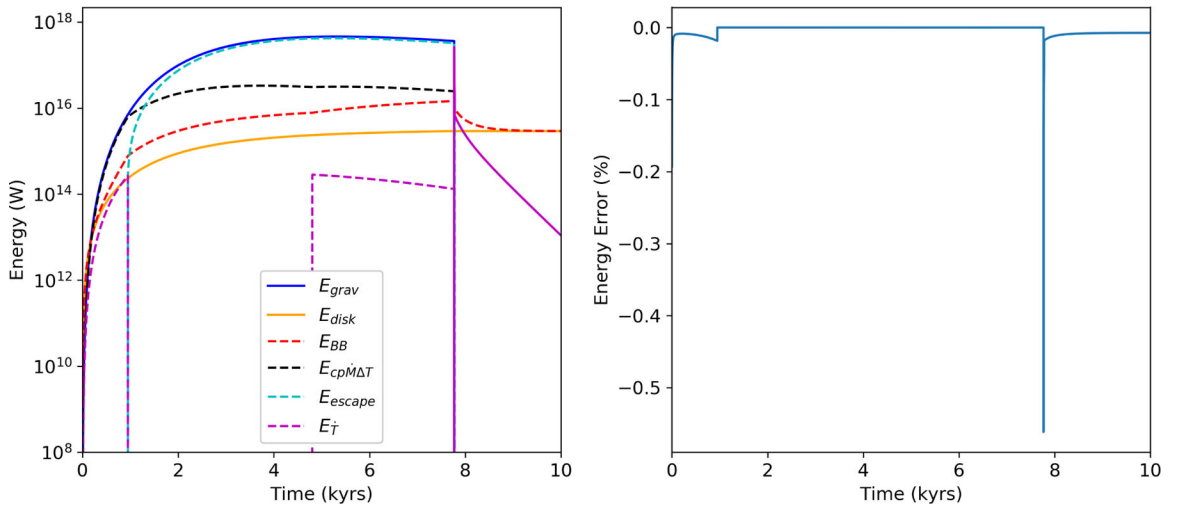
Figure 5.
left) Each of the model energy terms as a function of time for the model shown in Figure 1. E_{Grav} is the gravitational energy accretion, E_{disk} is the incoming radiation from the disk, E_{BB} is the blackbody radiation from the surface. Solid lines indicate energy sources (for the surface) and dashed lines are sinks. right) Error in the energy conservation with time. The mean energy error in this run is 0.003% (median is 0.0 to within machine precision).

D.2. Saturated case methods

The equations for the saturated case used in this work are fully derived in Lehmer et al. (2017). Here we just discuss the key assumptions of the derivation and the numerical implementation. For the derivation itself see Appendix 2 of Lehmer et al. (2017).

For this derivation the temperature structure of the atmosphere is assumed to be in saturated vapor pressure (SVP) equilibrium. The SVP of water is approximated as

$$p = p_w e^{-T_w/T} \tag{D20}$$

Here p_w and T_w are experimentally determined constants. We use $T_w = 5200$ K and $p_w = 1.13 \times 10^6$ bar (Lehmer et al. 2017). Equation 9 can be written in a general form

$$\frac{1}{u}\frac{\partial u}{\partial r} = \frac{N}{D} \tag{D21}$$

In the saturated atmosphere these can be algebraically found to be

$$N = \frac{2RT}{r}\left(\frac{T_w}{T_w - T}\right) - \frac{GM}{r^2} \tag{D22}$$

$$D = u^2 - RT\left(\frac{T_w}{T_w - T}\right) \tag{D23}$$

As in the isothermal case we can solve for the location and conditions at the critical point where the velocity is equal to the local sound speed. These values are

$$r_c = \frac{GM}{2RT_c}\left(\frac{T_w - T_c}{T_w}\right) \tag{D24}$$

$$u_c^2 = RT_c\left(\frac{T_w - T_c}{T_w}\right) = \frac{GM}{2r_c^3} \tag{D25}$$

where T_c is the temperature at the critical point. The other condition needed to integrate Equation D21 is the $\left(\frac{\partial u}{\partial r}\right)_c$. This can be found via L'Hopital's rule to be (letting $x = \frac{1}{u}\frac{\partial u}{\partial r}$)

$$\left(2 + \frac{T_w T_c}{(T_w - T_c)^2}\right)x^2 + \frac{4}{r_c}\frac{T_w T_c}{(T_w - T_c)^2}x + \frac{4}{r_c^2}\frac{T_w T_c}{(T_w - T_c)^2} - \frac{2}{r_c^2} = 0 \tag{D26}$$

This equation can be solved for x via the quadratic equation. All these equations require knowledge of T_c however our model only tracks the surface temperature. Because of this an initial guess T_c is used and Equations 6 and D21 are integrated to the surface. This integration gives a surface temperate that can be compared to the model surface temperature for that timestep. Using the difference between these values, T_c is updated and the integration iterated until the integrated surface temperature is within 2 K.

D.3. Sensitivity

Figure 6 shows how the final density and fractionation results depend on the number of time steps used. For all the models presented in this work we use 10^6 timesteps with 10^5 saved in the output (used for the δD calculations).

Figure 7 shows how the final density and fractionation depend on the thickness of the surface layer z that is assumed to be in thermal equilibrium. So long $z < r$ the temperature during heating and escape is not sensitive to this value. The actual thickness of this layer will depend on the size and speed of impact at the surface as well as the depth and circulation of a surface ocean.
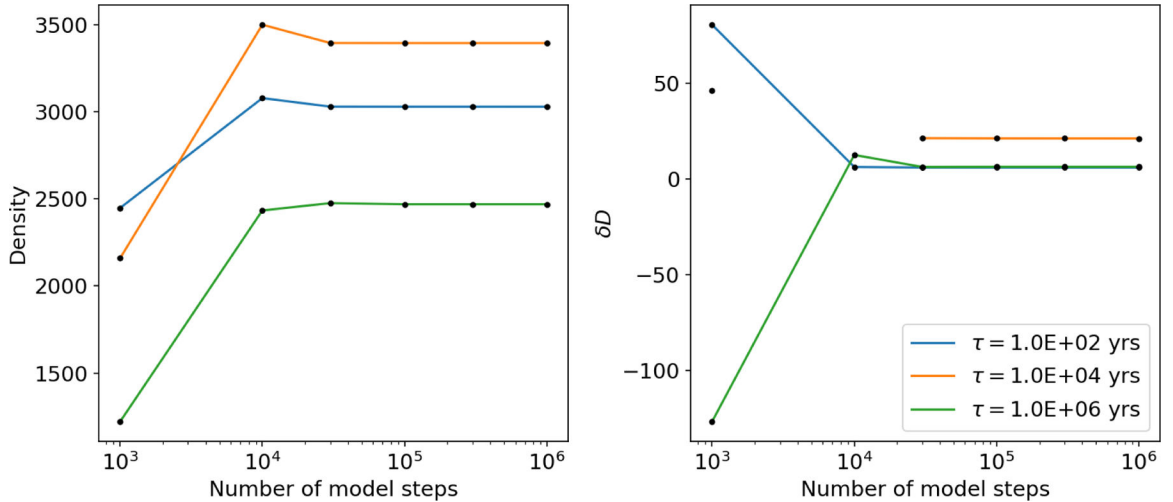
Figure 6.
Convergence of the final model density and δD. These runs use an isothermal atmosphere with $R_f = 2500$ km, $T_B = 250$ K, $p_B = 0.0$ Pa.
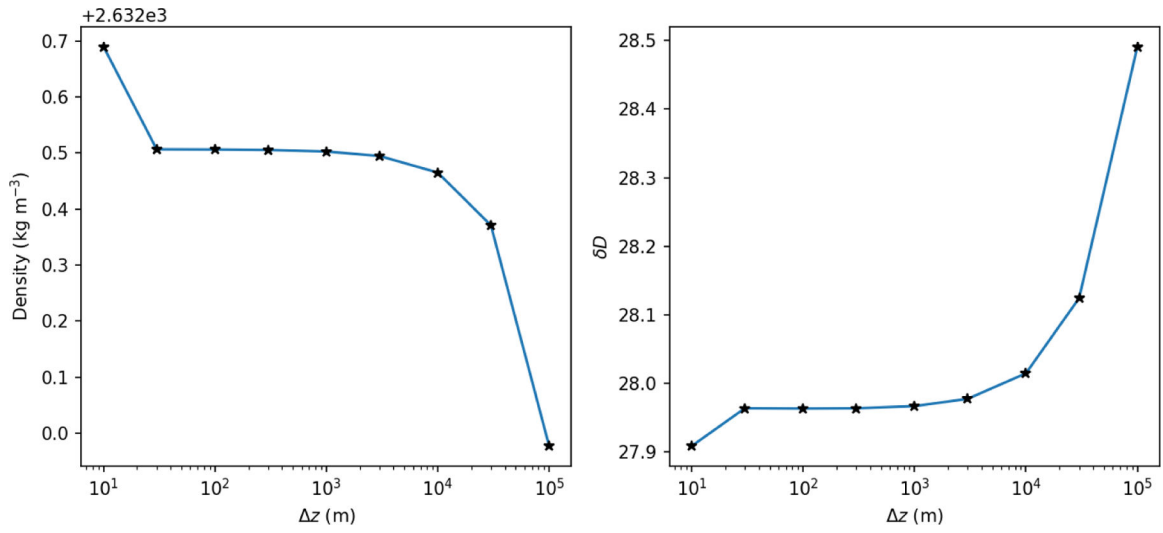
Figure 7.
Sensitivity of the final density and δD to the surface layer thickness (Δz). All other values are the same as Figure 1. The nominal value used throughout the work is 10^4 m.
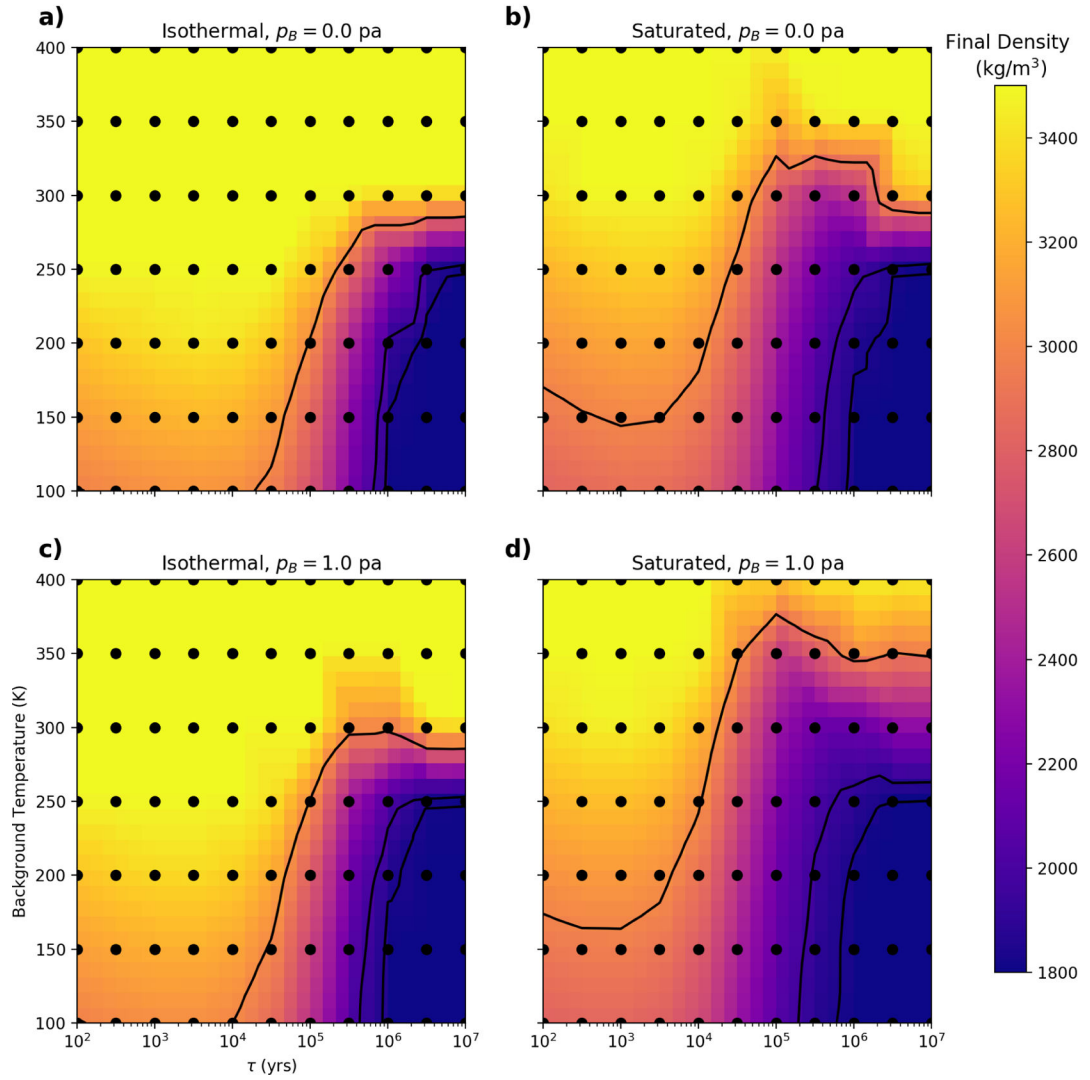
E.: ADDITIONAL FIGURES

$R_f = 2500$ km

Figure 8.

Final density results for model runs with $R_f = 2500$ km. Solid contours are the density of Europa, Ganymede and Callistio. This final radius produces worlds similar like Io, Ganymede, and Callistio but larger than Europa.

δD, $R_0 = 2000$ km
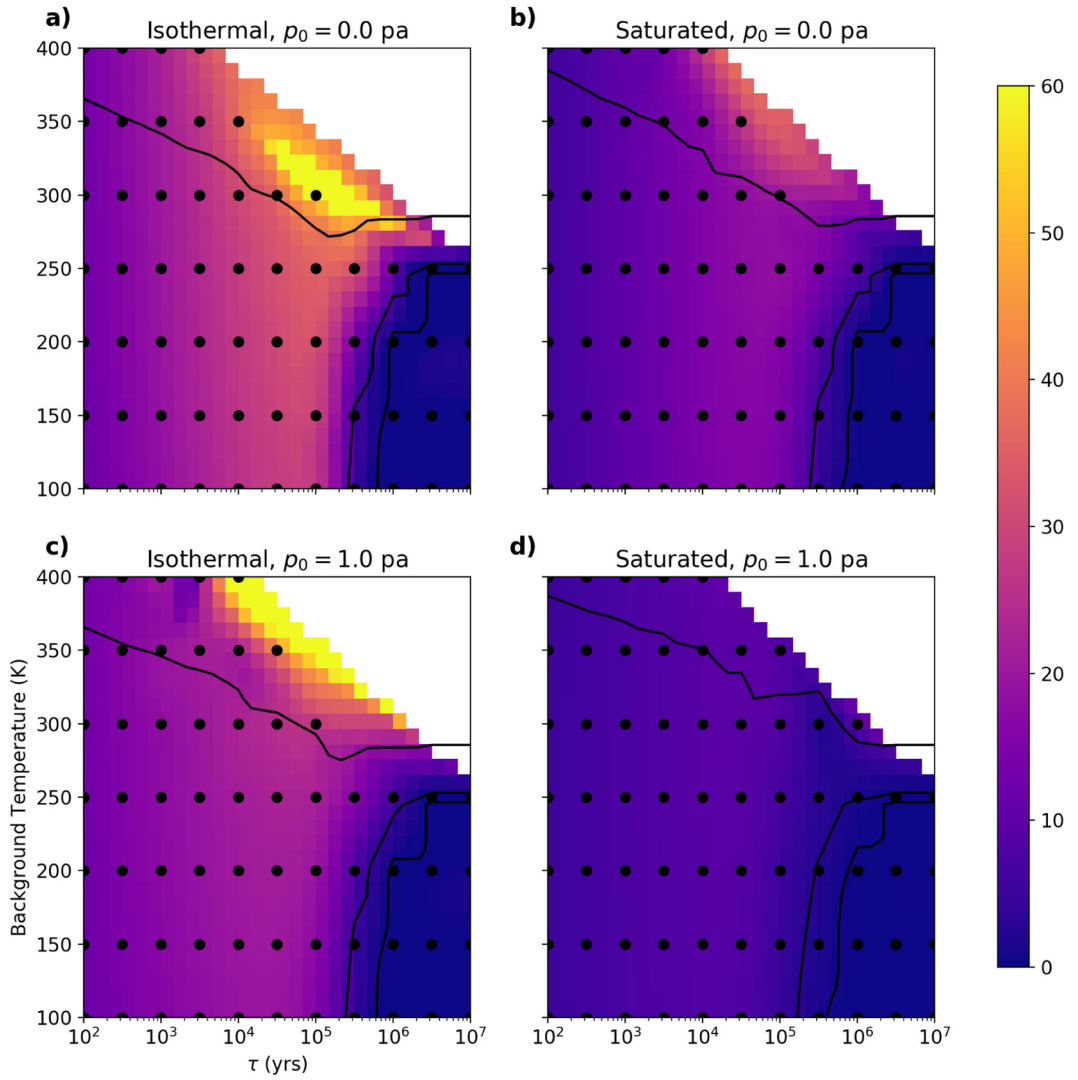
Figure 9.

Fractionation results (δD) for the runs presented in Figure 3. Note that runs that have no water remaining at the end of the run are not shown. The density contours from Figure 3 are superimposed.

δD, $R_0 = 2500$ km
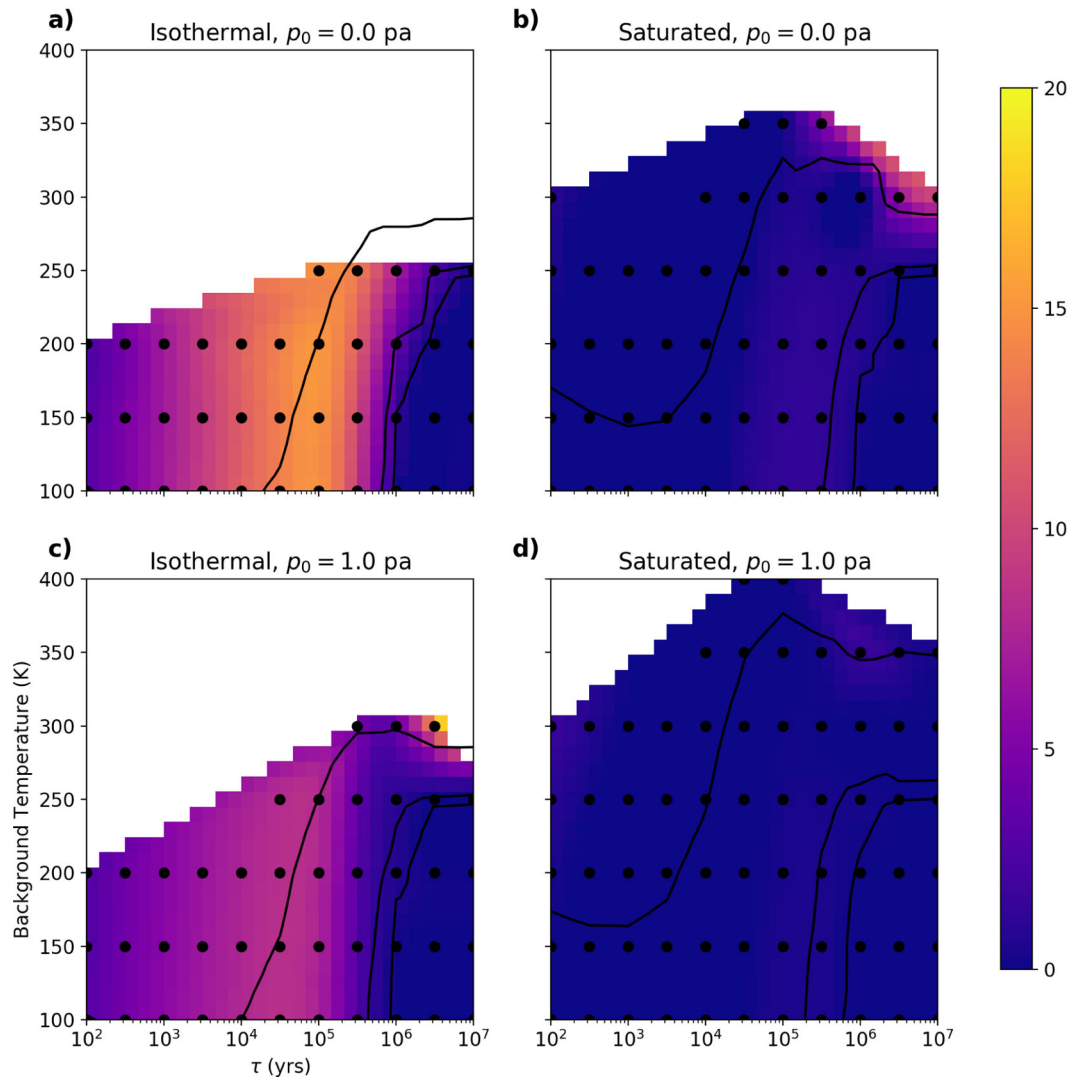
Figure 10.
Fractionation results for the runs presented in Figure 8.
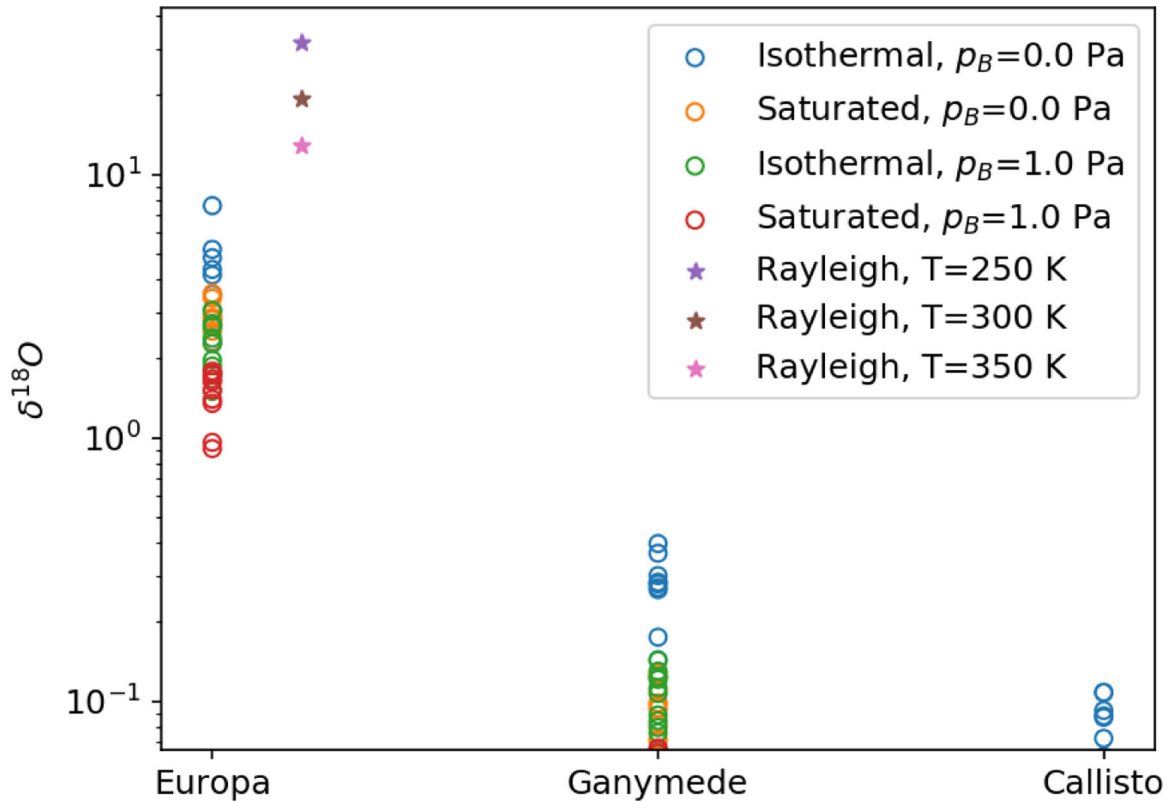
Figure 11.
Same as Figure 4 only for Oxygen isotopes

REFERENCES

Alibert Y, Mousis O, & Benz W 2005, A&A, 439, 1205

Asphaug E, & Reufer A 2013, Icarus, 223, 544

Barr AC, & Canup RM 2008, Icarus, 198, 163

Bierson C, & Nimmo F 2019, Icarus, 326, 10 [PubMed: 32139923]

Canup RM, & Ward WR 2002, The Astronomical Journal, 124, 3404

Canup RM, & Ward WR 2006, Nature, 441, 834 [PubMed: 16778883]

Canup RM, & Ward WR 2009, Europa, 59

Castillo-Rogez J, Vernazza P, & Walsh K 2019, Monthly Notices of the Royal Astronomical Society, 486, 538

Charnoz S, Crida A, Castillo-Rogez JC, et al. 2011, Icarus, 216, 535

Clark RN, Brown RH, Cruikshank DP, & Swayze GA 2019, Icarus, 321, 791

Dwyer C, Nimmo F, Ogihara M, & Ida S 2013, Icarus, 225, 390

Horita J, & Wesolowski DJ 1994, Geochimica et Cosmochimica Acta, 58, 3425

Hunten DM 1973, Journal of the Atmospheric Sciences, 30, 1481

Hunter JD 2007, Computing in Science & Engineering, 9, 90

Koll DDB, & Cronin TW 2018, Proceedings of the National Academy of Sciences, 115, 10293

Kuramoto K, & Matsui T 1994, Journal of Geophysical Research: Planets, 99, 21183

Lehmer OR, Catling DC, & Zahnle KJ 2017, The Astrophysical Journal, 839, 32

Lunine JI, & Stevenson DJ 1982, Icarus, 52, 14

Malamud U, & Prialnik D 2015, Icarus, 246, 21

McKinnon WB 1997, Icarus, 130, 540

Moore WB 2006, Icarus, 180, 141

Mosqueira I, & Estrada PR 2003a, Icarus, 163, 198

Mosqueira I, & Estrada PR 2003b, Icarus, 163, 232

Mozurkewich M 1986, Aerosol Science and Technology, 5, 223

Ogihara M, & Ida S 2012, The Astrophysical Journal, 753, 60

Pollack J, & Fanale F 1982, in Satellites of Jupiter, 872–910

Ronnet T, Mousis O, & Vernazza P 2017, The Astrophysical Journal, 845, 92

Roth L, Saur J, Retherford KD, et al. 2014, Science, 343, 171 [PubMed: 24336567]

Safranov, VS; 1972.

Schubert G, Anderson JD, Spohn T, & McKinnon WB 2004, Jupiter: The planet, satellites and magnetosphere, 1, 281

Shampine LF, & Gordon MK 1975, Computer solution of ordinary differential equations: the initial value problem (Freeman)

Showman AP, Stevenson DJ, & Malhotra R 1997, Icarus, 129, 367

Tian F, & Toon OB 2005, Geophysical Research Letters, 32, n/a, l18201

Tian F, Toon OB, Pavlov AA, & Sterck HD 2005, The Astrophysical Journal, 621, 1049

Vance S, Harnmeijer J, Kimura J, et al. 2007, Astrobiology, 7, 987 [PubMed: 18163874]

Virtanen P, Gommers R, Oliphant TE, et al. 2019, arXiv e-prints, arXiv:1907.10121

Waite HJ Jr., Lewis WS, Magee BA, et al. 2009, Nature, 460, 487

Young E, Shahar A, Nimmo F, et al. 2019, Icarus, 323, 1 [PubMed: 30739951]

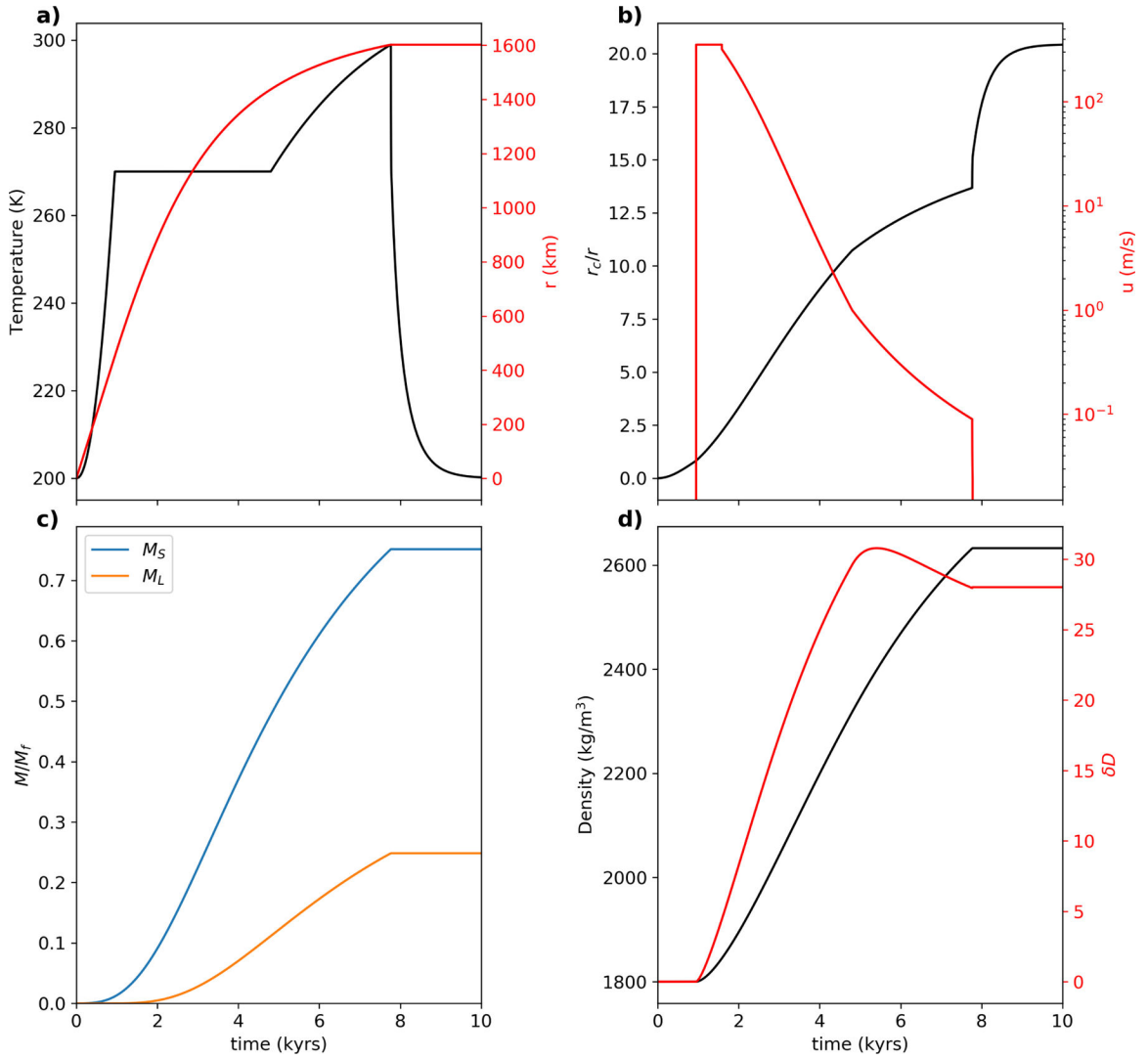Zahnle KJ, & Kasting JF 1986, Icarus, 68, 462

Figure 1.
An example model run for $\tau = 10$ kyr, $R_f = 2000$ km, $T_B = 200$ K, isothermal atmosphere, and no background pressure. a) Satellite surface temperature (black) and radius (red). b) Critical radius distance normalized by the body radius (black). This is a metric for the strength of hydrodynamic escape where lower values correspond to stronger escape. The surface vertical wind speed is shown in red. c) Mass of the satellite (M_S, blue) and total mass lost (M_L, orange) normalized by the final total mass ($M_S + M_L$). d) Satellite density (black) and hydrogen fractionation (red).
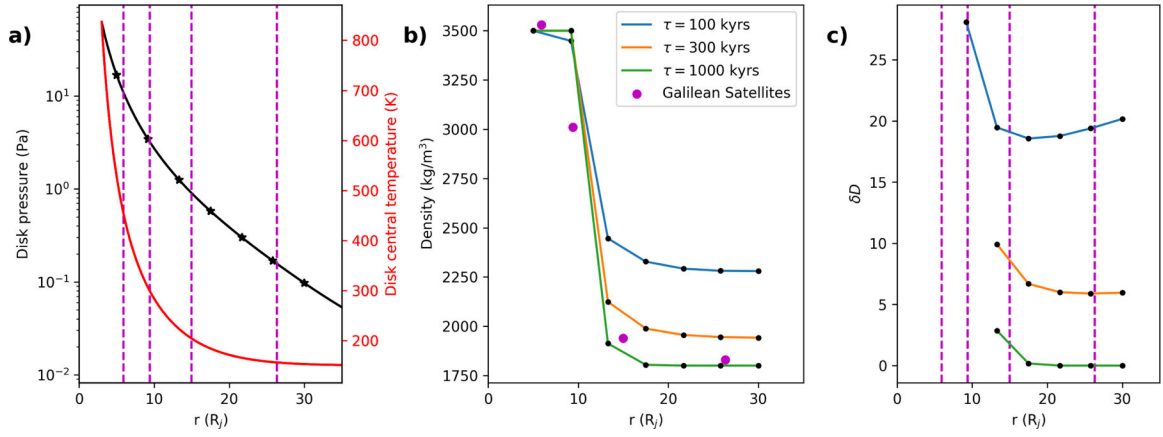
Figure 2.
a) Temperature and pressure conditions using Canup & Ward (2002) parameters $a = 5 \times 10^{-3}$, $M_J/\dot{M} = 10^8$ yrs, opacity=0.1 m²/kg. These are the same parameters used in Figure 6 of Canup & Ward (2002). Models were run with the parameters at the black stars. b) Observed density of the Galilian satellites (magenta) and the model results for three satellite accretion timescales. c) δD values in model runs. There is no value shown for models where no ice remains. In all plots the vertical dashed lines are the current orbital locations of the Galilean satellites.
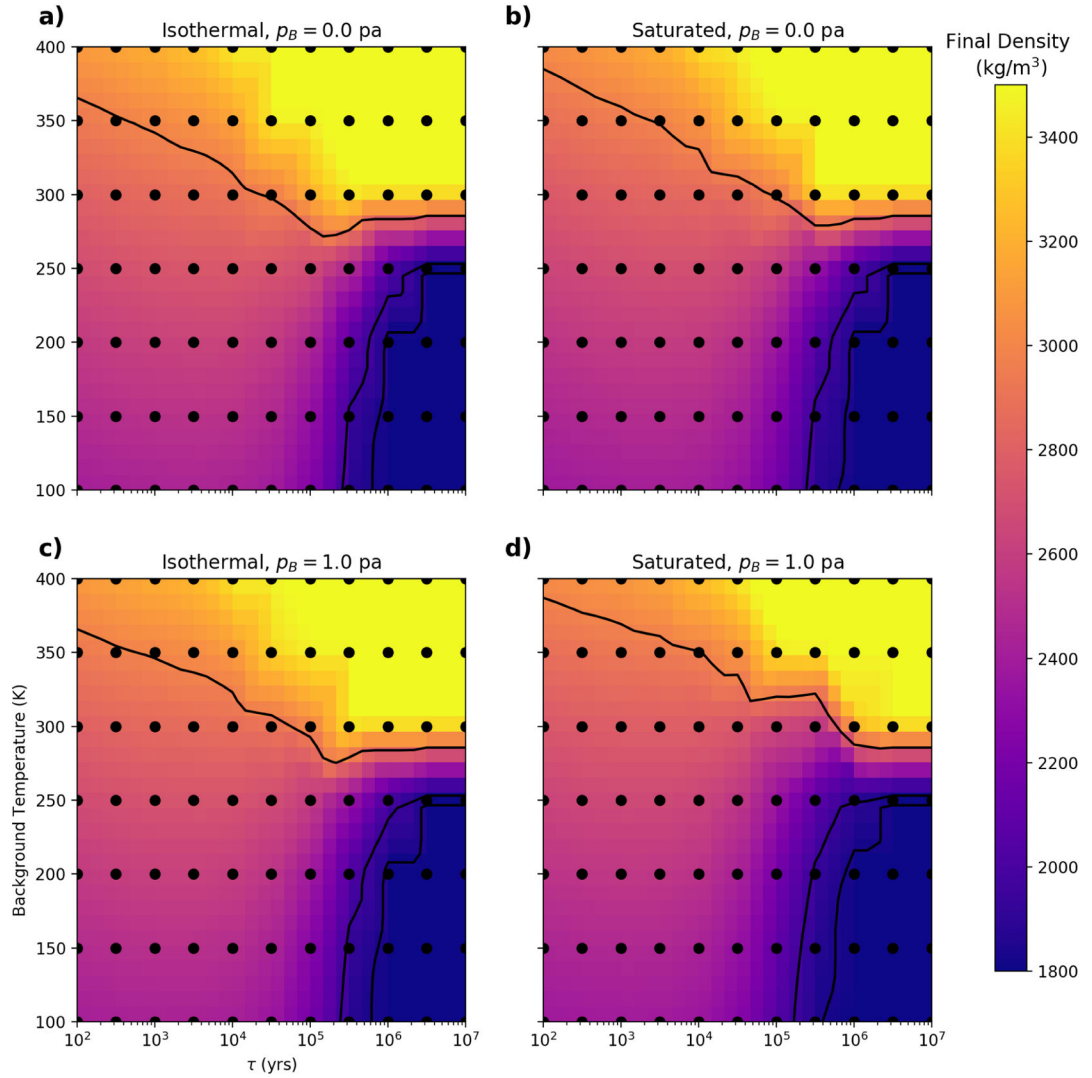
$R_f = 2000$ km

Figure 3.

Final density results for model runs with $R_f = 2000$ km. The density of the accreted material in all cases was 1800 kg/m^3. Each panel shows different assumptions about the atmospheric temperature structure (isothermal or saturated) and background disk pressure (zero or one pascal). Solid contours are the density of Europa, Ganymede, and Callisto. This final radius produces worlds with a radius comparable to Europa and smaller than the other satellites. An equivalent plot for larger radii is show in Figure 8.
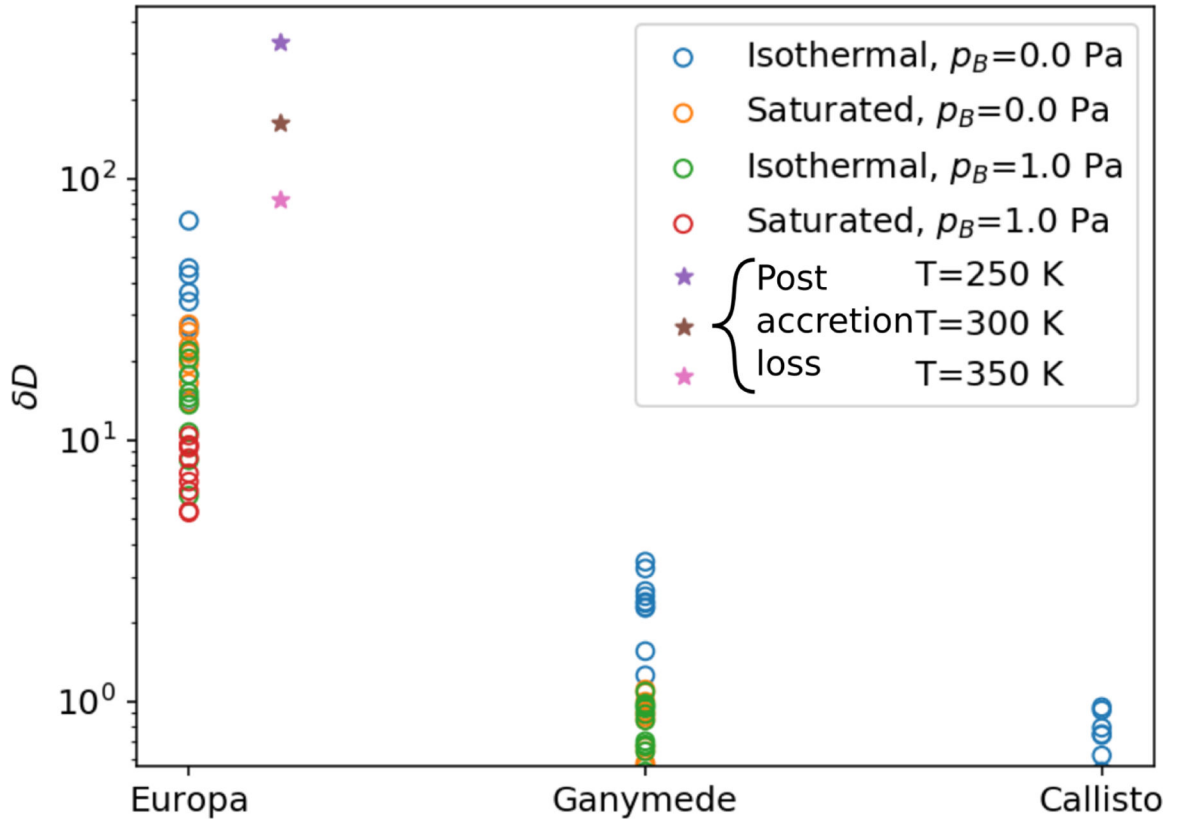
Figure 4.
Estimated δD values estimated by interpolating to the satellite densities across background temperature and formation timescale. Europa values use $R_f = 2000$ km while the Ganymede and Callisto values use $R_f = 2500$ km. Stars have the same fraction of ice lost as the other Europa points but assume that all the ice is initially accreted and subsequently lost with equilibrium (Rayleigh) liquid-vapor fractionation. An equivalent plot for $\delta^{18}O$ is shown in Figure 11. For reference the D/H measurement of Enceladus's plume by Cassini INMS in these units is $\delta D = 860^{+960}_{-450}$ (Waite Jr. et al. 2009).

Table 1.

Size and density of the Galilean Satellites (Schubert et al. 2004). Rock mass fractions calculated assuming an ice density of 920 and rock density of 3500 kg/m^3.

	Radius (km)	Density (kg/m^3)	Ice Mass Fraction
Io	1821.6	3530	-
Europa	1565.0	3010	5.8%
Ganymede	2631.2	1940	28.7%
Callisto	2410.3	1830	32.5%